

1 Editor's comments to the Author:

2 Please take into account the comments below to make a few minor corrections to your revised manuscript before publication.

3 Please also include the mandatory sections on data availability and author contribution.

4

5 We wish to express our appreciation for the editor for the careful comments and suggestions. We modified the manuscript  
6 following your suggestions one by one. The sections on data availability and author contribution are added before the  
7 acknowledgements. We refer Menviel et al (2017), which suggest weaker and shallower NADW and weaker AABW at the  
8 LGM from model-data comparison of  $\delta^{13}\text{C}$  and radiocarbon, in the end of Section 3.3. Our replies are highlighted gray.

9

10 Abstract: Please use only present tense. For example: L. 8: "We find", L.22: "Our model underestimates"

11

12 changed

13

14 P17, L. 62-63: "atmospheric CO<sub>2</sub> is not directly transferred to the deep ocean" Maybe you can rephrase as a "transfer of  
15 carbon from the atmosphere to the deep ocean"

16

17 changed following your suggestion

18

19 P23, L.27: "a slight EP increase is found"

20

21 changed

22

23 P24, L. 85: Please add reference to Khatiwala et al. accepted.

24

25 added

26

27 P25, L. 26: "a glacial CO<sub>2</sub> decrease of more than 30 ppm"

28

29 changed

30

31 P25, L. 31-p26, L. 48: "important for the atmospheric CO<sub>2</sub> response (Roth et al., 2014; Wallmann et al., 2016)."

32

33 changed as you suggested

34

35 P26, L. 52: “EP increases ...and...the nutrient increase are smaller”

36

37 **changed**

38

39 P28, L.36: “the underestimation of deoxygenation”

40

41 **changed**

42

43 P29, L.72: I would suggest to remove “In conclusion, “

44

45 **removed**

46

47 P29, L. 73: Please change “responsible for the glacial CO<sub>2</sub> decline of greater than 30 ppm” to “could explain a glacial CO<sub>2</sub>

48 decline of more than 30 ppm” or “decline greater than 30 ppm”

49

50 **The text is changed to “could explain a glacial CO<sub>2</sub> decline of more than 30 ppm”.**

51

52

53 **Glacial CO<sub>2</sub> decrease and deep-water deoxygenation by iron**  
54 **fertilization from glaciogenic dust**

55 Akitomo Yamamoto<sup>1,2</sup>, Ayako Abe-Ouchi<sup>1,2</sup>, Rumi Ohgaito<sup>1</sup>, Akinori Ito<sup>1</sup>, Akira Oka<sup>2</sup>

56 <sup>1</sup>Japan Agency for Marine-Earth Science and Technology, Yokohama, Japan

57 <sup>2</sup>Atmospheric and Ocean Research Institute, The University of Tokyo, Kashiwa, Japan

58

59 *Corresponding author:* A. Yamamoto (akitomo@jamstec.go.jp)

60 **Abstract**

61 Increased accumulation of respired carbon in the deep ocean associated with enhanced efficiency of the biological  
62 carbon pump is thought to be a key mechanism of glacial CO<sub>2</sub> drawdown. Despite greater oxygen solubility due to  
63 seawater cooling, recent quantitative and qualitative proxy data show glacial deep-water deoxygenation, reflecting  
64 increased respired carbon accumulation. However, the mechanisms of deep-water deoxygenation and contribution  
65 from the biological pump to glacial CO<sub>2</sub> drawdown have remained unclear. In this study, we report the significance of  
66 iron fertilization from glaciogenic dust in glacial CO<sub>2</sub> decrease and deep-water deoxygenation using our numerical  
67 simulation, which successfully reproduces the magnitude and large-scale pattern of the observed oxygen changes from  
68 the present to the Last Glacial Maximum. Sensitivity experiments show that physical changes contribute to only one-  
69 half of all glacial deep deoxygenation whereas the other one-half is driven by iron fertilization and an increase in the  
70 whole ocean nutrient inventory. We ~~find~~ that iron input from glaciogenic dust with higher iron solubility is the most  
71 significant factor in enhancing the biological pump and deep-water deoxygenation. Glacial deep-water deoxygenation  
72 expands the hypoxic waters in the deep Pacific and Indian oceans. The simulated global volume of hypoxic waters is  
73 nearly double the present value, suggesting that glacial deep-water was a more severe environment for benthic animals  
74 than that of the modern oceans. Our model ~~underestimates~~ the deoxygenation in the deep Southern Ocean because of  
75 enhanced ventilation. The model-proxy comparison of oxygen change suggests that a stratified Southern Ocean is  
76 required for reproducing the oxygen decrease in the deep Southern Ocean. Iron fertilization and a global nutrient  
77 increase contribute to a decrease in glacial CO<sub>2</sub> of more than 30 ppm, which is supported by the model-proxy agreement

削除: found

削除: ed

80 of oxygen change. Our findings confirm the significance of the biological pump in glacial CO<sub>2</sub> drawdown and  
81 deoxygenation.

82

### 83 1 Introduction

84 The oceanic carbon cycle has been proposed as a driver of glacial–interglacial CO<sub>2</sub> change; however, the magnitude of glacial  
85 CO<sub>2</sub> reduction of 80–100 ppm has yet to be fully reproduced by numerical model simulations using both an ocean general  
86 circulation model (OGCM) and a biogeochemical model (Ciais et al., 2013). The oceanic soft-tissue biological pump, by which  
87 the photosynthetic production, sinking, and remineralization of organic matter store dissolved inorganic carbon in the deep  
88 ocean, is among the mechanisms controlling glacial-interglacial as well as future atmospheric CO<sub>2</sub> change (Sarmiento and  
89 Gruber 2006; Sigman et al., 2010; Yamamoto et al., 2018). During glacial periods, the efficiency of the biological pump would  
90 have been enhanced by biogeochemical processes (e.g. dust-borne iron fertilization (Martin, 1990) and an increase in nutrient  
91 inventory associated with a sea-level drop (Broecker, 1982; Wallmann et al., 2016)), ~~leading to the transfer of carbon from the~~  
92 ~~atmosphere to the deep ocean.~~ Although changes in marine productivity during glacial periods and its relationship to the dust  
93 deposition flux have been widely supported by proxy records (Kohfeld et al., 2005; Jaccard et al., 2013), there are no direct  
94 proxy records of the greater accumulation of respired organic carbon. Thus, the contribution of the biological pump to glacial  
95 CO<sub>2</sub> reduction is poorly understood.

96  
97 Because the dissolved oxygen cycle is the mirror image of the biological carbon cycle (oxygen is produced by photosynthesis  
98 and is utilized with consistent stoichiometry through the remineralization of sinking organic matter in the ocean interior),  
99 oxygen is consumed in the ocean interior when respired organic carbon accumulates in seawater. Thus, reconstructed oxygen  
100 change is useful to constrain the biological pump magnitude and respired carbon accumulation. Proxy data show that, despite  
101 greater oxygen solubility due to lower sea surface temperatures (SSTs), oxygen concentrations decreased throughout the deep  
102 ocean during the Last Glacial Maximum (LGM) (Jaccard and Galbraith, 2012). This indicates greater oxygen consumption  
103 and respired carbon accumulation, which could have been caused by several processes including greater organic matter  
104 transport into the deep ocean, increasingly restricted air-sea exchange due to sea-ice expansion, and/or more sluggish ocean  
105 circulation. However, previous modeling studies have shown conflicting oxygen changes in LGM simulations (Galbraith and  
106 Jaccard, 2015; Schmittner and Somes, 2016; Buchanan et al., 2016; Bopp et al., 2017; Somes et al., 2017; Galbraith and de  
107 Lavergne, 2018) and the causes of the oxygen decrease in the deep ocean have not yet been fully explored.

删除: and thus

删除: atmospheric CO<sub>2</sub> would have been transported to the glacial deep ocean.

111  
112 Furthermore, because most observations provide only qualitative estimates of oxygen changes, previous model-proxy  
113 comparisons have only discussed the glacial oxygen trend (oxygenation in the upper ocean and deoxygenation in the deep  
114 ocean). Several recent studies using  $\delta^{13}\text{C}$  in benthic foraminiferal or iodine-to-calcium ratios in planktonic foraminifera were  
115 able to quantify oxygen concentration changes (Schmiedl and Mackensen, 2006; Hoogakker et al., 2015, 2018; Gottschalk et  
116 al., 2016; Lu et al., 2016; Bunzel et al., 2017; Umling and Thunell, 2018). These quantitative proxy data provide firmer  
117 constraints on respired carbon accumulation, such that a quantitative model-proxy comparison of oxygen change is very useful  
118 for quantifying the contribution of the biological pump to glacial  $\text{CO}_2$  drawdown.

119  
120 In this study, to quantify the impact of changes in the biological pump on glacial carbon and oxygen cycles, we conducted pre-  
121 industrial (PI) and LGM simulations using the coupled atmosphere–ocean general circulation model (Oka et al., 2011), aerosol  
122 model (Ohgaito et al., 2018), and ocean biogeochemical model (Yamamoto et al., 2015). We focused here on the iron  
123 fertilization process in enhancing the biological pump. We attempted to separately quantify iron fertilization effects from desert  
124 dust and glaciogenic dust (derived from glacier erosion). Previous studies using mineral aerosol models suggest that  
125 glaciogenic dust significantly contributed to an increase in the dust deposition flux at high latitudes during the LGM (e.g. the  
126 glaciogenic dust derived from Patagonian glaciers increased dust deposition in the Southern Ocean (SO)) and provided a LGM  
127 dust deposition flux distribution more consistent with the reported measurements (Mahowald et al., 2006; Ohgaito et al., 2018).  
128 Moreover, the iron solubility in glaciogenic dust (~3%) is much higher than that in desert dust (~1%) (Schroth et al., 2009);  
129 however, the higher solubility effect of glaciogenic dust on iron fertilization was not considered in previous modeling studies.  
130 Glaciogenic dust is a significant source of bioavailable iron (Shoenfelt et al., 2018) and would therefore have a major impact  
131 on biological productivity in high nutrient and low chlorophyll (HNLC) regions where biological productivity is limited by  
132 the lack of iron. We also considered the effect of an increase in macronutrients inventory associated with a glacial sea level  
133 drop of ~120 m (Broecker, 1982; Wallmann et al., 2016). A decrease in the area of continental margins reduced the burial of  
134 organic matter in margin sediments, leading to increases in the global inventory of phosphate ( $\text{PO}_4$ ) and nitrate ( $\text{NO}_3$ ). Based  
135 on a recent simulation, increases in  $\text{NO}_3$  and  $\text{PO}_4$  inventories by 15% can be assumed (Wallmann et al., 2016).

136  
137 We performed several sensitivity experiments as listed in Table 1 to explore the contribution of changes in atmospheric dust  
138 and nutrient inventory on glacial carbon and oxygen cycles. Moreover, our modeled oxygen changes were compared to recently  
139 reported qualitative (Jaccard and Galbraith, 2012) and quantitative reconstructions (Schmiedl and Mackensen, 2006;  
140 Hoogakker et al., 2015, 2018; Gottschalk et al., 2016; Lu et al., 2016; Bunzel et al., 2017; Umling and Thunell, 2018) to  
141 evaluate the simulated accumulation of respired carbon. Our simulation shows that glaciogenic dust and increased nutrient  
142 inventory play a crucial role in glacial CO<sub>2</sub> decrease and deep-water deoxygenation.

143

## 144 **2 Model and experiments**

145 The ocean biogeochemical cycle was calculated using the Model for Interdisciplinary Research on Climate (MIROC)-based  
146 offline biogeochemical model, based on Yamamoto et al. (2015), with the implementation of an iron cycle. A one box  
147 atmosphere is coupled to an offline biogeochemical model to predict atmospheric CO<sub>2</sub> concentration through gas exchange  
148 between the atmosphere and ocean surface. For the tracer calculation, the model uses prescribed monthly output data of  
149 horizontal ocean velocities, vertical diffusivity, temperature, salinity, sea surface height, sea surface wind speed, sea-ice  
150 fraction, and sea surface solar radiation derived from PI and LGM simulations conducted by Oka et al. (2011) using the MIROC  
151 4m AOGCM. Both PI and LGM simulations follow the PMIP2 protocol (Braconnot et al., 2007). MIROC 4m simulates the  
152 weaker and shallower Atlantic Meridional Overturning Circulation (AMOC) during the LGM (see Fig. 1 in Oka et al. (2011)),  
153 which is consistent with  $\delta^{13}\text{C}$  distributions reported from proxy data (Curry and Oppo, 2005). The horizontal and vertical  
154 resolutions of the offline biogeochemical model are the same as those in MIROC 4m.

155

156 This biogeochemical model includes two phytoplankton classes (nitrogen fixers and other phytoplankton), zooplankton,  
157 particulate detritus, nitrate (NO<sub>3</sub>), phosphate (PO<sub>4</sub>), dissolved iron (DFe), dissolved oxygen (O<sub>2</sub>), dissolved inorganic carbon  
158 (DIC), alkalinity (ALK), two carbon isotopes (<sup>13</sup>C and <sup>14</sup>C), and an ideal age tracer. The ideal age is set to zero at the surface  
159 and ages at a rate of 1 yr yr<sup>-1</sup> in the ocean interior. Constant stoichiometry relates the C, N, P, and DFe content of the biological  
160 variables and their exchanges to inorganic variables (NO<sub>3</sub>, PO<sub>4</sub>, DFe, O<sub>2</sub>, ALK, and DIC). The maximum phytoplankton growth

161 and microbial remineralization rates are assumed to increase with seawater temperature (Eppley, 1972). The iron cycle that is  
162 incorporated in the biogeochemical model mainly follows Parekh et al. (2005). In addition to dust deposition, which is assumed  
163 as the only DFe source in Parekh et al. (2005), sedimentary and hydrothermal DFe inputs are considered. When the DFe  
164 concentration exceeds the total ligand concentration, a formulation for the DFe scavenging rate of Moore and Braucher (2008)  
165 is applied. To obtain a realistic distribution of the iron-limited region, total ligand concentration, which controls the amount of  
166 the free form of iron, is set to a global constant value of  $0.6 \mu\text{mol m}^{-3}$  instead of the original value of  $1 \mu\text{mol m}^{-3}$  (Fig. 1a).

167  
168 Dust deposition flux is obtained from the monthly output data of MIROC-ESM in the PI and LGM simulations (Ohgaito et al.,  
169 2018). Dust is assumed to contain a constant fraction of iron (3.5 wt%); 1% of the iron in desert dust is assumed to  
170 instantaneously dissolve at the sea surface. The global DFe flux from dust in the PI is  $2.7 \text{ Gmol yr}^{-1}$  (Table 1). We used two  
171 sets of LGM dust deposition flux labelled as LGMctl and LGMglac as calculated in a previous study (Ohgaito et al., 2018).  
172 LGMctl is the standard LGM simulation, which has been submitted to Coupled Model Intercomparison Project Phase 5 /  
173 Paleoclimate Modelling Intercomparison Project (CMIP5/PMIP4). LGMglac is identical to LGMctl, except that an additional  
174 glaciogenic dust flux based on Mahowald et al. (2006) is included. In LGMctl, the dust deposition flux is underestimated in  
175 North America, Eurasia, the South Pacific, the SO, and Antarctica compared to the proxy data of ice and sediment cores  
176 (Kohfeld et al., 2013; Albani et al., 2014). Because glaciogenic dust increases dust deposition at high latitudes, the  
177 underestimation is generally improved in LGMglac (see Ohgaito et al., 2018, for more details). The global DFe fluxes from  
178 dust are  $8.6 \text{ Gmol yr}^{-1}$  and  $13.9 \text{ Gmol yr}^{-1}$  for LGMctl and LGMglac, respectively.

179  
180 Present observation generally shows a lower Fe solubility at a higher Fe concentration in aerosols and a higher solubility at a  
181 lower concentration (Fig. S1). A wider range of aerosol Fe solubility (from 0.2% to 48%) has been derived from observations  
182 over the SO, but different types of Fe-containing minerals such as pyrogenic Fe oxides can be considered to achieve high Fe  
183 solubilities (Ito et al., 2019). Thus, an assumed constant iron solubility of 2% in all types of dust could lead to overestimation  
184 of a total DFe flux from different types of Fe-containing aerosols during the LGM (Muglia et al., 2017). However, a much  
185 higher Fe solubility (1–42% of Fe solubility) as derived from observations for the LGM aerosols in Antarctica has suggested

186 that an assumed constant iron solubility of 1–2% for all types of dust could lead to a DFe flux underestimation during the LGM  
187 (Conway et al., 2015). In LGM\_glac3%, an iron solubility of 3% in glaciogenic dust is assumed (Schroth et al., 2009), such  
188 that the global DFe flux is 24.5 Gmol yr<sup>-1</sup>. This value is approximately 10 times larger than that of the PI simulation and is  
189 larger than a recent estimation, suggesting that a quadrupling of the global DFe flux is constrained by a model-proxy  
190 comparison of δ<sup>15</sup>N and δ<sup>13</sup>C (Muglia et al., 2018). As with the present DFe input from dust, glacial DFe input has large  
191 uncertainties. As an upper estimate of the DFe flux from dust, we set the iron solubility at 10% in glaciogenic dust in  
192 LGM\_glac10%.

193  
194 The DFe input flux from the sediments is estimated based on Moore and Braucher (2008). We assumed that the sedimentary  
195 DFe flux is proportional to the flux of organic carbon reaching the sea floor. To consider the realistic bathymetry of the  
196 continental shelves, the iron flux is weighted by the fraction of bottom area of the ETOPOV2 data that falls within the bounds  
197 of the model grid cell. The global DFe flux from the sediments in the PI is 33.1 Gmol yr<sup>-1</sup>. In the LGM simulations, the DFe  
198 input from sedimentary sources changes according to the flux of organic carbon reaching the sea floor. A decrease in the DFe  
199 input from sedimentary sources because of a sea-level drop is not considered. Muglia et al. (2017) showed this effect causes a  
200 CO<sub>2</sub> increase of 15 ppm. The hydrothermal DFe flux is regulated by the ridge spreading rate, as parameterized by a constant  
201 DFe/Helium ratio (Tagliabue et al., 2010). The hydrothermal DFe flux in the PI is ~8.5 Gmol yr<sup>-1</sup>. In the LGM simulations,  
202 the DFe input from hydrothermal sources is the same as that from PI.

203  
204 The biogeochemical model was initialized from annual mean climatology data based on the World Ocean Atlas 2009  
205 (WOA2009: Garcia et al., 2010a and 2010b) for dissolved NO<sub>3</sub>, PO<sub>4</sub>, and O<sub>2</sub> and the Global Ocean Data Analysis Project (Key  
206 et al., 2004) for DIC and ALK. The initial DFe concentration is a constant value of 0.6 nM. For the spin-up, the last 50 years  
207 of data in the MIROC PI experiments were cyclically applied to the offline ocean biogeochemical model. The model was spun  
208 up for more than 3000 years with a prescribed atmospheric CO<sub>2</sub> concentration of 285 ppm to eliminate model drift in the global  
209 inventory of all tracers. Similar to Yamamoto et al. (2015), all physical and biogeochemical tracers, except salinity and

210 dissolved iron, have correlation coefficients with observational data greater than 0.85 and normalized standard deviation values  
211 between 0.7 and 1.1.

212  
213 LGM experiments were run for 3000 years, following 3000 years of spin-up under PI conditions. The atmospheric CO<sub>2</sub>  
214 concentration was predicted. We increased the salinity, PO<sub>4</sub>, and NO<sub>3</sub> inventory by 3% to account for the reduced ocean  
215 volume because of the sea level drop. All experiments are listed in Table 1. LGM\_clim uses LGM boundary conditions.  
216 LGM\_dust is based on LGM\_clim but uses the dust deposition flux of LGMctf. Similarly, LGM\_glac3% and LGM\_glac10%  
217 use the dust deposition flux of LGMglac, but with an iron solubility of glaciogenic dust of 3% and 10%, respectively. LGM\_all  
218 is similar to LGM\_glac3%, but the NO<sub>3</sub> and PO<sub>4</sub> inventories are increased by 15%. This assumption is based on a recent model  
219 simulation that shows a ~15% increase in nutrient inventory is caused by reduced organic matter burial in shallow sediments  
220 associated with a sea level drop (Wallmann et al., 2016). In our simulations, changes in benthic denitrification were not  
221 considered. Somes et al. (2017) show that a decrease in benthic denitrification because of a sea level drop reduces NO<sub>3</sub> loss  
222 and thus leads to a larger NO<sub>3</sub> inventory in the LGM ocean. We analyzed the results from the last 100 years of each simulation.  
223

## 224 **3 Results and Discussion**

### 225 **3.1 Glacial nutrient cycles and export production**

226 In the LGM\_clim, which uses LGM climate boundary conditions, the NO<sub>3</sub> redistribution induced by weaker and shallower  
227 AMOC reduces nutrient supply from the deep ocean to the surface (Table 2 and Fig. 2). The NO<sub>3</sub> concentration in the euphotic  
228 zone decreases by 12% and the global export production (EP) is reduced by 0.54 Pg C yr<sup>-1</sup> compared to that of the PI simulation.  
229 Corresponding to the surface NO<sub>3</sub> decrease, significant EP decreases are found in the North Atlantic and North Pacific (Fig.  
230 3a and Fig. S2). However, the surface DFe concentration slightly changes. Because these changes in DFe and NO<sub>3</sub> decrease  
231 the iron-limited areas by 27% (Fig. 1b), the simulated LGM climate tends to mitigate the impacts of iron fertilization on  
232 biological productivity and the carbon cycle.

233

234 To evaluate the impacts of desert and glaciogenic dust on the ocean biogeochemical cycles, we conducted sensitivity studies.  
235 The DFe input from desert dust with a 1% iron solubility was applied in LGM\_dust, whereas glaciogenic dust with 3% or 10%  
236 iron solubility was additionally applied in LGM\_glac3% or LGM\_glac10%, respectively. Iron fertilization from only desert  
237 dust has a limited impact on the EP. Iron fertilization from both desert and glaciogenic dust increases the EP by 0.88 Pg C yr<sup>-1</sup>  
238 south of 45°S whereas the EP decreases by 0.86 Pg C yr<sup>-1</sup> north of 45°S, where most oceans are nitrogen-limited regions  
239 (LGM\_glac3% – LGM\_clim; Table 2). Enhanced primary production consumes the NO<sub>3</sub> of the euphotic zone in the SO and  
240 its anomaly is transported to the Antarctic bottom water (AABW). Subsequently, the surface NO<sub>3</sub> reduction in the SO is also  
241 transported to low-latitude regions via surface and intermediate waters (Fig. 2), thus reducing the EP in nitrogen-limited regions  
242 at low latitudes. Remarkable EP reductions occur north of the iron-limited regions of the SO (Fig. 3b). Our results demonstrate  
243 that enhanced biotic carbon export in the SO is partly compensated for by reduced carbon export in low-latitude regions. From  
244 the comparison between the effect of desert dust (LGM\_dust – LGM\_clim) and that of glaciogenic dust (LGM\_glac3% –  
245 LGM\_dust), we found that an increase in the EP due to dust-borne iron fertilization in the SO is mainly caused by glaciogenic  
246 dust (Table 2).

247  
248 For 15% increases in NO<sub>3</sub> and PO<sub>4</sub> inventory associated with sea level drop (LGM\_all), the EP increases globally in the  
249 nitrogen-limited regions, leading to a global EP increase of 0.86 Pg C yr<sup>-1</sup> (LGM\_all – LGM\_glac3%; Table 2). Simulated EP  
250 changes from the PI are in good agreement with the paleoproductivity reconstruction (Kohfeld et al., 2013) (Fig. 3c). Among  
251 the common patterns is the north-south dipole pattern in the SO with an EP decrease at higher latitudes and an EP increase at  
252 lower latitudes. The EP decrease at higher latitudes is attributed to sea ice expansion and the associated reduction of surface  
253 shortwave radiation (Oka et al., 2011) whereas iron fertilization increases the EP at lower latitudes. In the model, the EP  
254 changes also have an east-west dipole pattern; a slight EP increase is found in the South Pacific Ocean and significant EP  
255 increases occur in the South Atlantic and Indian oceans. We found that this pattern is attributed to iron fertilization by  
256 glaciogenic dust. Glaciogenic dust derived from Patagonian glaciers is transported to the South Atlantic and Indian oceans by  
257 the southern westerly wind; however, it is unable to reach the South Pacific (Fig. S3). Proxy data show no clear east-west  
258 dipole pattern, suggesting that the model underestimates iron fertilization in the Pacific sector of the Southern Ocean. However,

删除: s

删除: are

261 proxy data in the South Pacific remain sparse and a quantitative comparison of EP changes between the South Atlantic and  
262 South Pacific is limited. Therefore, further proxy data in the South Pacific is required for a comprehensive understanding of  
263 the glacial EP changes and iron fertilization.

264

### 265 **3.2 CO<sub>2</sub> reduction and its relationship to efficiency of the biological pump and dust flux**

266 Climate change reduces the atmospheric CO<sub>2</sub> concentration by 26.4 ppm (LGM\_clim – PI, Table 2), which is similar to that  
267 of previous simulations (Chikamoto et al., 2012; Menviel et al., 2012; Kobayashi et al., 2015). Circulation changes (i.e. a  
268 weaker and shallower AMOC and AABW expansion) cause DIC to decrease in the upper ocean and increase below 2000 m  
269 depth, such that the vertical DIC gradient between the surface and deep oceans is enhanced (Fig. 4). The efficiency of the  
270 oceanic biological pump is calculated following Ito and Follows (2005). The global mean preformed PO<sub>4</sub> is the difference  
271 between the total globally averaged PO<sub>4</sub> and global mean remineralized PO<sub>4</sub>,  $P_{pref} = P_{tot} - P_{remi}$ . Here,  $P_{pref}$  is the preformed  
272 PO<sub>4</sub> concentration,  $P_{tot}$  is the total PO<sub>4</sub> concentration, and  $P_{remi}$  is the remineralized PO<sub>4</sub> concentration. The remineralized PO<sub>4</sub>  
273 is given by  $P_{remi} = AOU \times R_{P:O}$ , where  $R_{P:O}$  is a constant phosphorous to oxygen ratio, and AOU is apparent oxygen utilization.  
274 A decrease in preformed PO<sub>4</sub> and thus an increase in remineralized PO<sub>4</sub> indicate an increase in the efficiency of the oceanic  
275 biological pump. Although globally integrated EP decreases, circulation change and deepening of the remineralization profile  
276 due to seawater cooling (Matsumoto, 2007) reduce the preformed nutrient inventory, enhancing the efficiency of the biological  
277 pump (Table 2). The enhanced accumulation of respired carbon associated with the more efficient biological pump and  
278 increased CO<sub>2</sub> solubility from the lower SST contribute to a decreased CO<sub>2</sub>. Notably, the AOU is different from true oxygen  
279 utilization due to the air-sea disequilibrium which is on the order of 20 mmol m<sup>-3</sup> in deep-water formation regions (Russell and  
280 Dickson, 2003; Duteil et al., 2013). Changes in surface ocean disequilibrium between the PI and LGM simulations might lead  
281 to large errors in the AOU changes (Khatriwala et al., accepted).

282

283 Iron fertilization from desert and glaciogenic dust enhances the vertical DIC gradient and causes a CO<sub>2</sub> reduction of 1.2 ppm  
284 (LGM\_dust – LGM\_clim) and 15.6 ppm (LGM\_glac3% – LGM\_dust), respectively. Our results show that the glacial CO<sub>2</sub>  
285 reduction due to dust-bone iron fertilization is mainly driven by glaciogenic dust. A simulated total CO<sub>2</sub> reduction of 16.8 ppm

286 induced by iron fertilization is within the range of previous studies using OGCM or Earth system Models of Intermediate  
287 Complexity (EMICs) (8-25 ppm CO<sub>2</sub> drawdown (Bopp et al., 2003; Parekh et al., 2006; Tagliabue et al., 2009; Oka et al.,  
288 2011; Menviel et al., 2012; Lambert et al., 2015; Heinze et al., 2016; Muglia et al., 2017). DFe supply from dust also contributes  
289 to the glacial CO<sub>2</sub> reduction through enhanced efficiency of the biological pump (Table 2). The simulated atmospheric CO<sub>2</sub>  
290 concentration is proportionally reduced to the preformed PO<sub>4</sub> (Fig. 5a), similar to previous simulations under the present  
291 climate (Ito and Follows, 2005; Marinov et al., 2008). Figure 5b shows the CO<sub>2</sub> change in response to the DFe input magnitude.  
292 The iron fertilization efficiency to reduce CO<sub>2</sub> decreases with increasing DFe flux. This nonlinear response is driven by a  
293 decrease in the iron-limited areas and the associated weakening of the iron fertilization effect on EP (Fig. 5c). Because the  
294 iron-limited region dramatically decreases in size and the CO<sub>2</sub> difference between LGM\_glac3% and LGM\_glac10% is small,  
295 the CO<sub>2</sub> reduction of 20 ppm in LGM\_glac10% is near the upper limit (i.e. there are no iron-limited regions and thus no  
296 additional CO<sub>2</sub> reduction).

297  
298 The simulated upper limit of CO<sub>2</sub> reduction resulting from iron fertilization is not a robust result because present iron models  
299 have large uncertainty. While Parekh et al. (2008) show an upper limit of 10 ppm, other simulations show CO<sub>2</sub> decrease by  
300 greater than 20 ppm (Oka et al., 2011; Muglia et al., 2017). To obtain a better understanding of the impact of iron fertilization  
301 on glacial CO<sub>2</sub> decrease, the variability of the upper limit among iron models should be investigated in a future study.

302  
303 Increases in nutrient inventory from lower sea levels drive an additional CO<sub>2</sub> drawdown by 16 ppm (LGM\_all – LGM\_glac3%).  
304 We found that changes in the biological pump induced by iron fertilization and an increase in nutrient inventory contribute to  
305 a glacial CO<sub>2</sub> decrease of more than 30 ppm. The resultant total CO<sub>2</sub> reduction is ~60 ppm, which our model does not reproduce  
306 as the full variation in the glacial-interglacial CO<sub>2</sub> change. Note that changes in the sedimentation process (i.e. carbonate  
307 compensation and burial-nutrient feedback) are not considered in our simulation. The simulated increase in the bottom water  
308 DIC (Fig. 4) would enhance calcium carbonate dissolution in the sediments and thereby increase ocean alkalinity, leading to  
309 a further CO<sub>2</sub> decrease (Bouttes et al., 2011; Brovkin et al., 2012; Kobayashi et al., 2018). The long-term balance between the  
310 burial of organic material and nutrient input through weathering is also potentially important for the atmospheric CO<sub>2</sub> response

删除: greater

312 (Roth et al., 2014; Wallmann et al., 2016). For example, Tschumi et al. (2011) show that the nutrient-burial feedback  
313 significantly amplifies the effect of an increase in the  $\text{PO}_4$  inventory on the glacial  $\text{CO}_2$  decrease. Menviel et al. (2012)  
314 quantified the implication of ocean-sediment-lithosphere coupling for factorial experiments with an altered iron fertilization  
315 and altered  $\text{PO}_4$  inventory from transient glacial-interglacial simulations. Considering that EP increases due to iron fertilization  
316 and the nutrient increase are smaller in our simulations than that in previous studies (Tschumi et al., 2011; Menviel et al.,  
317 2012), the effect of burial-nutrient feedback on the glacial  $\text{CO}_2$  reduction may be smaller than previously estimated. As  
318 described in the next section, to assess the simulated accumulation of respired carbon, we compared the simulated oxygen  
319 changes to qualitative and quantitative proxy records.

320

### 321 3.3 Model-proxy comparison of glacial oxygen changes

322 Compared to the compilation of qualitative and quantitative proxy records of oxygen change from the Holocene to Last Glacial  
323 Maximum, LGM\_clim shows an increase in oxygen for the entire SO and underestimates deoxygenation in the deep Pacific  
324 and Indian oceans, in contrast to the proxy records (Fig. 6a). However, LGM\_all successfully reproduces large-scale spatial  
325 patterns of oxygen change, including for the SO (Fig. 6b). Moreover, the simulated changes in oxygen concentration agree  
326 well with quantitative reconstructions: a 45-65  $\text{mmol m}^{-3}$  decrease in the deep North Atlantic (Hoogakker et al., 2015), an ~30-  
327 80  $\text{mmol m}^{-3}$  decrease in the eastern equatorial Pacific (Hoogakker et al., 2018; Umling and Thunell, 2018), and a >80  $\text{mmol}$   
328  $\text{m}^{-3}$  in the upper SO of the Pacific sector (Lu et al., 2016). Our results clearly show the importance of iron fertilization and an  
329 increase in nutrient inventory in global deep deoxygenation. These model-proxy agreements of oxygen change support the  
330 simulated  $\text{CO}_2$  decrease of 30 ppm by the biological pump. However, the reconstructed  $\text{O}_2$  decrease of ~175  $\text{mmol m}^{-3}$  in the  
331 deep SO (Gottschalk et al., 2016) is much greater than the simulated decrease of ~30  $\text{mmol m}^{-3}$  from LGM\_all; thus, the  
332 respired carbon accumulation in the deep SO is underestimated in our model. This may be one of the reasons why the glacial-  
333 interglacial  $\text{CO}_2$  change of ~100 ppm cannot be reproduced in our simulations.

334

335 To clarify the mechanism of  $\text{O}_2$  change from LGM\_all – PI, we decomposed the  $\text{O}_2$  change into changes in saturation ( $\text{O}_{2\text{sat}}$ )  
336 and apparent oxygen utilization (AOU), where  $\Delta\text{O}_2 = \Delta\text{O}_{2\text{sat}} - \Delta\text{AOU}$ .  $\text{O}_{2\text{sat}}$  is computed from simulated seawater temperature

删除: in atmospheric  $\text{CO}_2$  and related tracers to changes in ocean biological cycles

删除: is

340 and salinity and AOU by subtracting the  $O_2$  concentration from  $O_{2sat}$ . Ocean cooling increases  $O_{2sat}$  globally, increasing the  
341 global mean value by  $25.5 \text{ mmol m}^{-3}$  (Fig. 7a). As with the  $O_2$  change,  $\Delta AOU$  shows a contrast between the upper and deep  
342 oceans (Fig. 7b). At a depth of 0-800 m, the AOU decreases by  $5.2 \text{ mmol m}^{-3}$  north of  $45^\circ\text{S}$ , which results from the decrease  
343 in biological oxygen consumption associated with EP reduction and increased ventilation (Fig. 7f). Therefore, the combined  
344 effects of an  $O_{2sat}$  increase and AOU decrease contribute to an overall  $O_2$  increase in the upper ocean. In the deep ocean ( $>2$   
345 km depth), the sum of AOU increases by  $72.8 \text{ mmol m}^{-3}$  (LGM\_all in Table 2), overcoming the  $O_{2sat}$  increase, resulting in  
346 deep  $O_2$  depletion. The relationship between changes in the  $O_2$  concentration,  $O_{2sat}$ , and AOU are consistent with that of a  
347 previous simulation (Bopp et al., 2017).

348  
349 The  $\Delta AOU$  is also decomposed into effects of climate change (LGM\_clim – PI), iron fertilization (LGM\_glac3% – LGM\_clim)  
350 and an increase in nutrient inventory (LGM\_all – LGM\_glac3%). The effects of climate change, circulation change, restricted  
351 air-sea gas exchange from sea-ice expansion, and deepening of remineralization due to seawater cooling leads to the AOU  
352 increasing by  $37.3 \text{ mmol m}^{-3}$  in the deep ocean (Table 2). In the deep North Atlantic, the simulated water mass age is older in  
353 the LGM than in the PI by up to 500 years, suggesting reduced ventilation (Fig. 7f). Therefore, significant AOU increases  
354 occur (Fig. 7c). Meanwhile, in the SO and deep Pacific Ocean, an increase in ventilation tends to decrease the AOU and thus  
355 partly compensates for the increase in the AOU. Regarding the effects of iron fertilization and nutrient inventory, the EP  
356 changes associated with iron fertilization and an increase in nutrient inventory enhance biological oxygen consumption and  
357 thus increase the AOU by  $21.4$  and  $14.1 \text{ mmol m}^{-3}$  in the deep ocean, respectively (Table 2 and Fig. 7d, e). In particular,  
358 glaciogenic dust causes an increase in the AOU of  $19.8 \text{ mmol m}^{-3}$ . Our results demonstrate that in addition to climate change,  
359 enhanced biological oxygen consumption associated with iron fertilization and increased nutrient inventory are crucial drivers  
360 of glacial deoxygenation in the deep ocean. While some previous modelling studies show deep ocean oxygenation during the  
361 LGM (Buchanan et al., 2016; Galbraith and Lavergne, 2018), this study and others reproduce deep ocean deoxygenation  
362 (Galbraith and Jaccard, 2015; Schmittner and Somes, 2016; Bopp et al., 2017; Somes et al., 2017). The conflicting oxygen  
363 change between the previous simulations can be attributed to different treatments of enhanced biological oxygen consumption

364 because iron fertilization and increased nutrient inventory are not considered in these simulations that fail to reproduce deep  
365 deoxygenation (Buchanan et al., 2016; Galbraith and Lavergne, 2018).

366

367 Glacial oxygen change expands the volume of hypoxic waters (defined here as  $[O_2] < 80 \text{ mmol m}^{-3}$ ) below 1000 m depth, such  
368 that the simulated global volume increases from the present value of 120 Mkm<sup>3</sup> to 237 Mkm<sup>3</sup> in LGM\_all. Significant  
369 expansion occurs in the deep Pacific and Indian oceans (Fig. 8), with hypoxic waters also appearing in the upper SO in the  
370 Pacific sector, consistent with proxy records (Hoogakker et al., 2018; Lu et al., 2016). Because hypoxic conditions are lethal  
371 for more than one-half of marine benthic animals (Vaquer-Sunyer and Duarte, 2008), expansion of hypoxic water in the deep  
372 ocean can have an adverse impact on benthic fauna. Determining the biotic responses to glacial expansion of hypoxic water  
373 would be helpful for understanding the biotic response to future deoxygenation associated with global warming.

374

375 Finally, we discuss [the](#) underestimation of deoxygenation in the deep SO in LGM\_all. Because simulated changes in the  
376 biological pump and sea-ice distributions are consistent with reconstructions (Obase et al., 2017), we then addressed circulation  
377 changes. The simulated water mass age of the deep SO is younger during the LGM than during the PI by ~200 years (Fig. 7f),  
378 indicating an increase in ventilation. However,  $\Delta^{14}\text{C}$  records show an increase in water mass age of more than 1000 years, and  
379 thus increased stratification (Skinner et al., 2010; Burke and Robinson, 2012). Enhanced mixing of surface waters with deep  
380 waters supplies oxygen-rich surface waters to the deep ocean and simultaneously releases carbon accumulated in the deep  
381 water to the atmosphere. Therefore, we attribute the underestimation of deoxygenation and carbon accumulation in the deep  
382 SO to overestimated ventilation. Our results suggest that a stratified SO is required for reproducing glacial CO<sub>2</sub> drawdown and  
383 oxygen decline in the deep SO, consistent with recent paleo-proxy data and models (Fischer et al., 2010; Sigman et al., 2010;  
384 Kobayashi et al., 2015; [Menviel et al., 2017](#)). [Menviel et al \(2017\) showed that weaker and shallower North Atlantic Deep](#)  
385 [Water and weaker AABW could be necessary to reproduce the LGM oceanic  \$\delta^{13}\text{C}\$  and radiocarbon distribution.](#)

386

387 **4 Conclusion and remarks**

388 We quantified the impacts on glacial deoxygenation and CO<sub>2</sub> decreases caused by glaciogenic dust with higher iron solubility  
389 and increase in nutrient inventory associated with a sea-level drop using the coupled atmosphere–ocean general circulation  
390 model, aerosol model, and ocean biogeochemical model. As a result, we successfully reproduced the magnitude and large-  
391 scale pattern of the observed oxygen change between the present and LGM. Our results show that iron fertilization from  
392 glaciogenic dust and an increase in nutrient inventory could explain a glacial CO<sub>2</sub> decline of more than 30 ppm and  
393 approximately one-half of deep ocean deoxygenation. These results also demonstrate the usefulness of the quantitative model-  
394 proxy comparison of oxygen change in understanding glacial-interglacial CO<sub>2</sub> change. However, large uncertainty remains  
395 because of the limited number of proxy data of quantitative oxygen change. Thus, we anticipate our findings will encourage  
396 studies to obtain further qualitative and quantitative reconstructions from throughout the global deep ocean. A comparison  
397 between the models and other proxy data (e.g. δ<sup>13</sup>C, (Schmittner and Some, 2016)) is also required to obtain a more robust  
398 and comprehensive understanding of the glacial carbon cycle.

399  
400 The changes in nutrient inventory during the LGM have large uncertainties. Previous studies estimate that the oceanic PO<sub>4</sub> and  
401 NO<sub>3</sub> inventories could have been 15–40% (Tamburini and Föllmi, 2009; Wallmann et al., 2016) and 10-100% (Deutsch et al.,  
402 2004; Eugster et al., 2013; Some et al., 2017) greater during glacial compared to interglacial periods, respectively. Moreover,  
403 Some et al. (2017) shows that sedimentary δ<sup>15</sup>N records provide no constrain on this effect. Future simulations should test the  
404 biogeochemical sensitivity to nutrient inventory changes.

405  
406 We focused on the impacts of DFe flux changes from the dust on glacial CO<sub>2</sub> drawdown and deoxygenation in this study.  
407 However, changes in the sedimentary and hydrothermal DFe flux and ligand concentration that are not considered in this study  
408 could also be important. A glacial sea-level drop decreases the sedimentary DFe flux due to the continental shelf reduction.  
409 However, the hydrothermal DFe flux is increased by the lower sea level and bottom pressure (Middleton et al., 2016). Muglia  
410 et al. (2017) show that the changes in sedimentary and hydrothermal DFe flux associated with a sea-level drop increase CO<sub>2</sub>  
411 by 15 ppm and decrease CO<sub>2</sub> by 6 ppm, respectively. Although sedimentary DFe flux is proportional to the organic carbon  
412 flux reaching the seafloor in our model, a parametrization with the Dfe flux as a function of organic carbon flux and bottom

删除: In conclusion, o

删除: are responsible for the

删除: greater

416 oxygen concentrations is proposed in Dale et al. (2015). Glacial deep-water deoxygenation would increase sedimentary DFe  
417 flux, leading to a further CO<sub>2</sub> decrease via the biological pump. Ligand concentrations strongly control DFe concentrations  
418 (Gledhill and Buck, 2012). Because the ligand concentration is affected by numerous factors (Völker and Tagliabue, 2015),  
419 changes in ligand concentration from the PI to LGM have large uncertainty. Thus, we quantified the effect of DFe flux changes  
420 under a constant ligand concentration in the PI and LGM simulations. Changes in the sedimentary and hydrothermal DFe flux  
421 and ligand concentration should be the subject of future research.

422  
423 Our model-proxy comparison shows the importance of the combination of a more sluggish SO circulation and enhanced  
424 biological transport of organic matter in the increased accumulation of respired carbon and deoxygenation in the deep SO.  
425 However, present climate models cannot reproduce the stratified SO. A possible reason is that they are too coarse to capture  
426 the process of dense water formation on the Antarctic shelf and tend to underestimate the strength of stratification in the SO  
427 (Heuzé et al., 2013). The brine rejection process and/or change in the vertical diffusion coefficient could be necessary to  
428 reproduce the stratified SO (Kobayashi et al., 2015; Bouttes et al., 2011). Similar to glacial oxygen changes, changes in ocean  
429 circulation in the SO are crucial in projecting future oxygen changes associated with global warming (Yamamoto et al., 2015).  
430 Therefore, an understanding of glacial oxygen changes will aid in better understanding and predicting future oxygen changes.  
431

432 **Data availability.** [Data are freely available from the corresponding author \(akitomo@jamstec.go.jp\) upon request.](#)

433

434 **Author contributions.** [AY and AA-O designed the research. AY conducted, and analysed experiments and prepared the paper.](#)

435 [AA-O provided the results of MIROC. RO provided the results of MIROC-ESM. All authors discussed the results and gave](#)

436 [their inputs on the manuscript.](#)

437

#### 438 **Acknowledgements**

439 [We thank the Editor Laurie Menviel as well as Fortunat Joos and Andreas Schmittner for their helpful comments.](#) This work

440 was supported by the Integrated Research Program for Advancing Climate Models ([TOUGOU programme](#)) from the

441 Ministry of Education, Culture, Sports, Science and Technology ([MEXT](#)), Japan, and JSPS KAKENHI grant number

442 17H06323. The simulations with the offline biogeochemical model were performed using the Fujitsu PRIMEHPC FX10

443 system in the Information Technology Center, University of Tokyo.

444

445

#### 446 **References**

447 Albani, S., Mahowald, N. M., Perry, A. T., Scanza, R. A., Zender, C. S., Heavens, N. G., Maggi, V., Kok, J. F., and Otto-

448 Bliesner, B. L.: Improved dust representation in the Community Atmosphere Model, *J. Adv. Model. Earth Sy.*, 6,

449 541–570, <https://doi.org/10.1002/2013ms000279>, 2014.

450 Bopp, L., Kohfeld, K. E., and Le Qu'ere, C.: Dust impact on marine biota and atmospheric CO<sub>2</sub> during glacial periods,

451 *Paleoceanography*, 18, 1046, doi:10.1029/2002PA000810, 2003.

452 Bopp, L., Resplandy, L., Orr, J. C., Doney, S. C., Dunne, J. P., Gehlen, M., Halloran, P., Heinze, C., Ilyina, T., Séférian, R.,

453 Tjiputra, J., and Vichi, M.: Multiple stressors of ocean ecosystems in the 21st century: projections with CMIP5

454 models, *Biogeosciences*, 10, 6225–6245, <https://doi.org/10.5194/bg-10-6225-2013>, 2013.

455 Bopp, L., Resplandy, L., Untersee, A., Le Mezo, P., and Kageyama, M.: Ocean (de)oxygenation from the Last Glacial  
456 Maximum to the twenty-first century: insights from Earth System models, *Philos. T. Roy. Soc. Lond. A*, 375, 2102,  
457 <https://doi.org/10.1098/rsta.2016.0323>, 2017.

458 Bouttes, N., Paillard, D., Roche, D. M., Brovkin, V., and Bopp, L.: Last Glacial Maximum CO<sub>2</sub> and  $\delta^{13}C$  successfully  
459 reconciled, *Geophys. Res. Lett.*, 38, L02705, doi:10.1029/2010gl044499, 2011.

460 Braconnot, P., Otto-Bliesner, B., Harrison, S., Joussaume, S., Peterchmitt, J.-Y., Abe-Ouchi, A., Crucifix, M., Driesschaert,  
461 E., Fichefet, Th., Hewitt, C. D., Kageyama, M., Kitoh, A., Lainé, A., Loutre, M.-F., Marti, O., Merkel, U., Ramstein,  
462 G., Valdes, P., Weber, S. L., Yu, Y., and Zhao, Y.: Results of PMIP2 coupled simulations of the Mid-Holocene and  
463 Last Glacial Maximum – Part 1: experiments and large-scale features, *Clim. Past*, 3, 261–277, doi:10.5194/cp-3-  
464 261-2007, 2007.

465 Broecker, W. S.: Glacial to interglacial changes in ocean chemistry, *Progress in Oceanography*, 11, 151–197,  
466 doi:10.1016/0079-6611(82)90007-6, 1982.

467 Brovkin, V., Ganopolski, A., Archer, D., and Munhoven, G.: Glacial CO<sub>2</sub> cycle as a succession of key physical and  
468 biogeochemical processes, *Clim. Past*, 8, 251-264, <https://doi.org/10.5194/cp-8-251-2012>, 2012.

469 Buchanan, P. J., Matear, R. J., Lenton, A., Phipps, S. J., Chase, Z., and Etheridge, D. M.: The simulated climate of the Last  
470 Glacial Maximum and insights into the global marine carbon cycle, *Clim. Past*, 12, 2271-2295,  
471 <https://doi.org/10.5194/cp-12-2271-2016>, 2016.

472 Bunzel, D., Schmiedl, G., Lindhorst, S., Mackensen, A., Reolid, J., Romahn, S., and Betzler, C.: A multi-proxy analysis of  
473 Late Quaternary ocean and climate variability for the Maldives, Inner Sea, *Clim. Past*, 13, 1791-1813,  
474 <https://doi.org/10.5194/cp-13-1791-2017>, 2017.

475 Burke, A. and Robinson, L. F.: The Southern Ocean's role in carbon exchange during the last deglaciation, *Science*, 335,  
476 557–561, 2012.

477 Chikamoto, M. O., Abe-Ouchi, A., Oka, A., Ohgaito, R., and Timmermann, A.: Quantifying the ocean's role in glacial CO<sub>2</sub>  
478 reductions, *Clim. Past*, 8, 545-563, <https://doi.org/10.5194/cp-8-545-2012>, 2012.

479 Ciais, P., Sabine, C., Bala, G., Bopp, L., Brovkin, V., Canadell, J., Chhabra, A., DeFries, R., Galloway, J., Heimann, M.,  
480 Jones, C., Le Quéré, C., Myneni, R. B., Piao, S., and Thornton, P.: Carbon and Other Biogeochemical Cycles, in:  
481 Climate Change 2013: The Physical Science Basis. Contribution of Working Group I to the Fifth Assessment Report  
482 of the Intergovernmental Panel on Climate Change, edited by: Stocker, T. F., Qin, D., Plattner, G.-K., Tignor, M.,  
483 Allen, S. K., Boschung, J., Nauels, A., Xia, Y., Bex, V., and Midgley, P. M., Cambridge University Press,  
484 Cambridge, United Kingdom and New York, NY, USA, 465– 570, 2013.

485 Conway, T., Wolff, E., Roethlisberger, R., Mulvaney, R., and Elderfield, H.: Constraints on soluble aerosol iron flux to the  
486 Southern Ocean at the Last Glacial Maximum, *Nature Communications*, 6, 1–9, doi:10.1038/ncomms8850, 2015.

487 Curry, W. B. and Oppo, D. W.: Glacial water mass geometry and the distribution of  $\delta^{13}\text{C}$  of  $\text{CO}_2$  in the western Atlantic  
488 Ocean, *Paleoceanography*, 20, PA1017, doi:10.1029/2004PA001021, 2005.

489 Deutsch, C., Sigman, D. M., Thunell, R. C., Meckler, A. N., and Haug, G. H.: Isotopic constraints on glacial/interglacial  
490 changes in the oceanic nitrogen budget, *Global Biogeochem. Cy.*, 18, GB4012, doi:10.1029/2003GB002189, 2004.

491 Diaz, R. J. and Rosenberg, R.: Spreading dead zones and consequences for marine ecosystems, *Science*, 321, 926–929, 2008.

492 Durand, A., Chase, Z., Noble, T. L., Bostock, H., Jaccard, S. L., Townsend, A. T., Bindoff, N. L., Neil, H., and Jacobsen, G.:  
493 Reduced oxygenation at intermediate depth of the southwest Pacific during the last glacial maximum, *Earth Planet.*  
494 *Sc. Lett.*, 491, 48–57, 2018.

495 Duteil, O., Koeve, W., Oeschlies, A., Bianchi, D., Galbraith, E., Kriest, I., and Matear, R.: A novel estimate of ocean oxygen  
496 utilisation points to a reduced rate of respiration in the ocean interior, *Biogeosciences*, 10(11), 7723–7738, doi:  
497 10.5194/bg-10-7723-2013, 2013.

498 Eppley, R. W.: Temperature and phytoplankton growth in the sea, *Fish. B.-NOAA*, 70, 1063–1085, 1972.

499 Eugster, O., Gruber, N., Deutsch, C., Jaccard, S. L., and Payne, M. R.: The dynamics of the marine nitrogen cycle across the  
500 last deglaciation, *Paleoceanography*, 28, 116–129, doi:10.1002/palo.20020, 2013.

501 Fischer, H., Schmitt, J., Luthi, D., Stocker, T. F., Tschumi, T., Parekh, P., Joos, F., Kohler, P., Volker, C., Gersonde, R.,  
502 Barbante, C., Le Floch, M., Raynaud, D., and Wolff, E.: The role of Southern Ocean processes in orbital and  
503 millennial  $\text{CO}_2$  variations – a synthesis, *Quaternary Sci. Rev.*, 29, 193–205, 2010.

504 Galbraith, E. and de Lavergne, C.: Response of a comprehensive climate model to a broad range of external forcings:  
505 relevance for deep ocean ventilation and the development of late Cenozoic ice ages, *Clim. Dynam.*,  
506 <https://doi.org/10.1007/s00382-018-4157-8>, 2018.

507 Galbraith, E. D. and Jaccard, S. L.: Deglacial weakening of the oceanic soft tissue pump: global constraints from  
508 sedimentary nitrogen isotopes and oxygenation proxies, *Quaternary Sci. Rev.*, 109, 38–48,  
509 doi:10.1016/j.quascirev.2014.11.012, 2015.

510 Garcia, H. E., Locarnini, R., Boyer, T., Antonov, J., Baranova, O., Zweng, M., and Johnson, D.: Volume 3: Dissolved  
511 Oxygen, Apparent Oxygen Utilization, and Oxygen Saturation, *World Ocean Atlas 2009*, S. Levitus, Ed. NOAA  
512 Atlas NESDIS 70, US Government Printing Office, Washington, DC, 344 pp., 2010a.

513 Garcia, H. E., Locarnini, R., Boyer, T., Antonov, J., Zweng, M., Baranova, O., and Johnson, D.: Volume 4: Nutrients  
514 (phosphate, nitrate, silicate), *World Ocean Atlas 2009*, edited by: Levitus, S., NOAA Atlas NESDIS 71, US  
515 Government Printing Office, Washington, DC, 398 pp., 2010b.

516 Gledhill, M. and Buck, K.: The organic complexation of iron in the marine environment: a review, *Frontiers in*  
517 *Microbiology*, 3, 1–17, doi:10.3389/fmicb.2012.00069, 2012.

518 Gottschalk, J., Skinner, L. C., Lippold, J., Vogel, H., Frank, N., Jaccard, S. L., and Waelbroeck, C.: Biological and physical  
519 controls in the Southern Ocean on past millennial-scale atmospheric CO<sub>2</sub> changes, *Nat. Commun.*, 7, 11539,  
520 doi:10.1038/ncomms11539, 2016.

521 Heinze, C., Hoogakker, B. A. A., and Winguth, A.: Ocean carbon cycling during the past 130 000 years – a pilot study on  
522 inverse palaeoclimate record modelling, *Clim. Past*, 12, 1949–1978, <https://doi.org/10.5194/cp-12-1949-2016>, 2016.

523 Heuzé, C., Heywood, K. J., Stevens, D. P., and Ridley, J. K.: Southern Ocean bottom water characteristics in CMIP5 models,  
524 *Geophys. Res. Lett.*, 40, 1409–1414, doi:10.1002/grl.50287, 2013.

525 Hoogakker, B. A. A., Elderfield, H., Schmiedl, G., McCave, I. N., and Rickaby, R. E. M.: Glacial–interglacial changes in  
526 bottom water oxygen content on the Portuguese margin, *Nat. Geosci.*, 8, 40–43, doi:10.1038/ngeo2317, 2015.

527 Hoogakker, B. A. A., Lu, Z., Umling, N., Jones, L., Zhou, X., Rickaby, R. E. M., Thunell, R., Cartapanis, O., and Galbraith,  
528 E.: Glacial expansion of oxygen-depleted seawater in the eastern tropical Pacific. *Nature*, 562 (7727), 410-413.  
529 10.1038/s41586-018-0589-x, 2018.

530 Ito, A., Myriokefalitakis, S., Kanakidou, M., Mahowald, N. M., Scanza, R. A., Hamilton, D. S., Baker, A. R., Jickells, T.,  
531 Sarin, M., Bikkina, S., Gao, Y., Shelley, R. U., Buck, C. S., Landing, W. M., Bowie, A. R., Perron, M. M. G., Guieu,  
532 C., Meskhidze, N., Johnson, M. S., Feng, Y., Kok, J. F., Nenes, A., and Duce, R. A.: Pyrogenic iron: The missing  
533 link to high iron solubility in aerosols, *Sci. Adv.*, 5, eaau7671, doi: 10.1126/sciadv.aau7671, 2019.

534 Ito, T. and Follows, M. J.: Preformed phosphate, soft tissue pump and atmospheric CO<sub>2</sub>, *J. Mar. Res.*, 63, 813–839, 2005.

535 Jaccard, S. L. and Galbraith, E. D.: Large climate-driven changes of oceanic oxygen concentrations during the last  
536 deglaciation, *Nat. Geosci.*, 5, 151–156, doi:10.1038/ngeo1352, 2012.

537 Jaccard, S. L., Hayes, C. T., Hodell, D. A., Anderson, R. F., Sigman, D. M., and Haug, G. H.: Two modes of change in  
538 Southern Ocean productivity over the past million years, *Science*, 339, 1419–1423, 2013.

539 Jaccard, S. L., Galbraith, E. D., Martínez-García, A., and Anderson, R. F.: Covariation of deep Southern Ocean oxygenation  
540 and atmospheric CO<sub>2</sub> through the last ice age, *Nature*, 530, 207–10, doi:10.1038/nature16514, 2016.

541 [Khaliwala, S., Schmittner, A., and Muglia, J.: Air-sea disequilibrium enhances ocean carbon storage during glacial periods,](#)  
542 [Sci. Adv., accepted.](#)

543 Key, R. M., Kozyr, A., Sabine, C. L., Lee, K., Wanninkhof, R., Bullister, J. L., Feely, R. A., Millero, F. J., Mordy, C., and  
544 Peng, T.-H.: A global ocean carbon climatology: Results from Global Data Analysis Project (GLODAP), *Global*  
545 *Biogeochem. Cy.*, 18, GB4031, <https://doi.org/10.1029/2004GB002247>, 2004.

546 Kobayashi, H., Abe-Ouchi, A., and Oka, A.: Role of Southern Ocean stratification in glacial atmospheric CO<sub>2</sub> reduction  
547 evaluated by a three-dimensional ocean general circulation model, *Paleoceanography*, 30, 1202–1216, 2015.

548 Kobayashi, H., and Oka, A.: Response of atmospheric pCO<sub>2</sub> to glacial changes in the Southern Ocean amplified by carbonate  
549 compensation. *Paleoceanography* 33, 1206-1229, 2018.

550 Kohfeld, K. E., Le Quéré, C., Harrison, S. P., and Anderson, R. F.: Role of marine biology in glacial-interglacial CO<sub>2</sub>  
551 cycles, *Science*, 308, 74–78, doi:10.1126/science.1105375, 2005.

552 Kohfeld, K. E., Graham, R. M., De Boer, A. M., Sime, L. C., Wolff, E. W., Le Quere, C., and Bopp, L.: Southern  
553 Hemisphere westerly wind changes during the Last Glacial Maximum: paleo-data synthesis, *Quaternary Sci. Rev.*,  
554 68, 76–95, <https://doi.org/10.1016/j.quascirev.2013.01.017>, 2013.

555 Lambert, F., Tagliabue, A., Shaffer, G., Lamy, F., Winckler, G., Farias, L., Gallardo, L., and De Pol-Holz, R.: Dust fluxes  
556 and iron fertilization in Holocene and Last Glacial Maximum climates, *Geophys. Res. Lett.*, 42, 6014–6023,  
557 doi:10.1002/2015gl064250, 2015.

558 Lu, Z., Hoogakker, B. A. A., Hillenbrand, C.-D., Zhou, X., Thomas, E., Gutchess, K. M., Lu, W., Jones, L., and Rickaby, R.  
559 E. M.: Oxygen depletion recorded in upper waters of the glacial Southern Ocean, *Nat. Commun.*, 7, 11146,  
560 <https://doi.org/10.1038/ncomms11146>, 2015.

561 Mahowald, N. M., Muhs, D. R., Levis, S., Rasch, P. J., Yoshioka, M., Zender, C. S., and Luo, C.: Change in atmospheric  
562 mineral aerosols in response to climate: last glacial period, preindustrial, modern, and doubled carbon dioxide  
563 climates, *J. Geophys. Res.*, 111, D10202, doi:10.1029/2005JD006653, 2006.

564 Marinov, I., Gnanadesikan, A., Sarmiento, J. L., Toggweiler, J. R., Follows, M., and Mignone, B. K.: Impact of oceanic  
565 circulation on biological carbon storage in the ocean and atmospheric pCO<sub>2</sub>, *Global Biogeochem. Cy.* 22(3),  
566 GB3007, doi:10.1029/2007GB002958, 2008.

567 Martin, J. H.: Glacial-interglacial CO<sub>2</sub> change: the iron hypothesis, *Paleoceanography*, 5, 1–13, 1990.

568 Matsumoto, K.: Biology-mediated temperature control on atmospheric pCO<sub>2</sub> and ocean biogeochemistry, *Geophys. Res.*  
569 *Lett.*, 34, L20605, <https://doi.org/10.1029/2007GL031301>, 2007.

570 Menviel, L., Joos, F., and Ritz, S. P.: Simulating atmospheric CO<sub>2</sub>, <sup>13</sup>C and the marine carbon cycle during the Last Glacial–  
571 Interglacial cycle: possible role for a deepening of the mean remineralization depth and an increase in the oceanic  
572 nutrient inventory, *Quat. Sci. Rev.*, 56, 46–68, [10.1016/j.quascirev.2012.09.012](https://doi.org/10.1016/j.quascirev.2012.09.012), 2012.

573 [Menviel, L., Yu, J., Joos, F., Mouchet, A., Meissner, K., and England, M.: Poorly ventilated deep ocean at the Last Glacial](#)  
574 [Maximum inferred from carbon isotopes: A data-model comparison study, \*Paleoceanography\*, 32, 2–17, 2017.](#)

575 Middleton, J. L., Langmuir, C. H., Mukhopadhyay, S., McManus, J. F., and Mitrovica, J. X.: Hydrothermal iron flux  
576 variability following rapid sea level changes, *Geophys. Res. Lett.*, 43, 3848–3856,  
577 <https://doi.org/10.1002/2016GL068408>, 2016.

578 Moore, J. K. and Braucher, O.: Sedimentary and mineral dust sources of dissolved iron to the world ocean, *Biogeosciences*,  
579 5, 631–656, doi:10.5194/bg-5-631-2008, 2008.

580 Moore, C. M., Mills, M. M., Arrigo, K. R., Berman-Frank, I., Bopp, L., Boyd, P. W., Galbraith, E. D., Geider, R. J., Guieu,  
581 C., Jaccard, S. L., Jickells, T. D., La Roche, J., Lenton, T. M., Mahowald, N. M., Marañón, E., Marinov, I., Moore,  
582 J. K., Nakatsuka, T., Oschilles, A., Saito, M. A., Thingstad, T. F., Tsuda, A., and Ulloa, O.: Processes and patterns of  
583 oceanic nutrient limitation, *Nat. Geosci.*, 6, 701–710, <https://doi.org/10.1038/ngeo1765>, 2013.

584 Muglia, J., Somes, C., Nickelsen, L., and Schmittner, A.: Combined effects of atmospheric and seafloor iron fluxes to the  
585 glacial ocean. *Paleoceanography* 32, 1204–1218, 2017.

586 Muglia, J., Skinner, L. C., and Schmittner A.: Weak overturning circulation and high Southern Ocean nutrient utilization  
587 maximized glacial ocean carbon, *Earth Planet Sc Lett*, 496, 47-56, doi: 10.1016/j.epsl.2018.05.038, 2018.

588 Obase, T., Abe-Ouchi, A., Kushara, K., Hasumi, H., and Ohgaito, R.: Responses of basal melting of Antarctic ice shelves to  
589 the climatic forcing of the Last Glacial Maximum and CO<sub>2</sub> doubling. *J. Climate*, 30, 3473–3497, 2017.

590 Ohgaito, R., Abe-Ouchi, A., O'ishi, R., Takemura, T., Ito, A., Hajima, T., Watanabe, S., and Kawamiya, M.: Effect of high  
591 dust amount on surface temperature during the Last Glacial Maximum: a modelling study using MIROC-ESM,  
592 *Clim. Past*, 14, 1565-1581, <https://doi.org/10.5194/cp-14-1565-2018>, 2018.

593 Oka, A., Abe-Ouchi, A., Chikamoto, M. O., and Ide, T.: Mechanisms controlling export production at the LGM: Effects of  
594 changes in oceanic physical field and atmospheric dust deposition, *Global Biogeochem. Cy.*, 25, GB2009,  
595 doi:10.1029/2009GB003628, 2011.

596 Parekh, P., Follows, M. J., and Boyle, E. A.: Decoupling of iron and phosphate in the global ocean, *Global Biogeochem. Cy.*,  
597 19, GB2020, doi:10.1029/2004GB002280, 2005.

598 Parekh, P., Follows, M. J., Dutkiewicz, S., and Ito, T.: Physical and biological regulation of the soft tissue carbon pump,  
599 *Paleoceanography*, 21, PA3001, doi:10.1029/2005PA001258, 2006.

600 Parekh, P., Joos, F., and Muller, S. A.: A modeling assessment of the interplay between aeolian iron fluxes and ironbinding  
601 ligands in controlling carbon dioxide fluctuations during Antarctic warm events, *Paleoceanography*, 23, Pa4202,  
602 doi:10.1029/2007pa001531, 2008.

603 Roth, R., Ritz, S. P., and Joos, F.: Burial-nutrient feedbacks amplify the sensitivity of atmospheric carbon dioxide to changes  
604 in organic matter remineralisation, *Earth Syst. Dynam.*, 5, 321-343, 10.5194/esd-5-321-2014, 2014.

605 Russell, J. L., and Dickson, A. G.: Variability in oxygen and nutrients in South Pacific Antarctic Intermediate Water, *Global*  
606 *Biogeochem Cy*, 17, doi:10.1029/2000gb001317, 2003.

607 Sarmiento, J. L., and Gruber, N.: *Ocean Biogeochemical Dynamics*, chap. 8, Carbon cycle, pp.318-358, Princeton Univ.  
608 Press, Princeton, N. J, 2006.

609 Schmiedl, G. and Mackensen, A.: Multispecies stable isotopes of benthic foraminifers reveal past changes of organic matter  
610 decomposition and deepwater oxygenation in the Arabian Sea, *Paleoceanography*, 21, 1–14,  
611 doi:10.1029/2006PA001284, 2006.

612 Schmittner, A. and Somes, C. J.: Complementary constraints from carbon (C-13) and nitrogen (N-15) isotopes on the glacial  
613 ocean's soft-tissue biological pump, *Paleoceanography*, 31, 669–693, 2016.

614 Schroth, A. W., Crusius, J., Sholkovitz, E. R., and Bostick, B. C.: Iron solubility driven by speciation in dust sources to the  
615 ocean, *Nat. Geosci.*, 2, 337–340, 2009.

616 Shoenfelt, E. M., Winckler, G., Lamy, F., Anderson, R. F., and Bostick, B. C.: Highly bioavailable dust-borne iron delivered  
617 to the Southern Ocean during glacial periods. *Proc. Natl. Acad. Sci. USA*, 115, 11180-11185, 2018

618 Sigman, D. M., Hain, M. P., and Haug, G. H.: The polar ocean and glacial cycles in atmospheric CO<sub>2</sub> concentration, *Nature*,  
619 466, 47–55, doi:10.1038/nature09149, 2010.

620 Skinner, L. C., Fallon, S., Waelbroeck, C., Michel, E., and Barker, S.: Ventilation of the deep Southern Ocean and deglacial  
621 CO<sub>2</sub> rise, *Science*, 328, 1147–1151, 2010.

622 Somes, C. J., Schmittner, A., Muglia, J., and Oschlies A.: A Three-Dimensional Model of the Marine Nitrogen Cycle during  
623 the Last Glacial Maximum Constrained by Sedimentary Isotopes, *Frontiers in Marine Science*, 4,  
624 doi:10.3389/fmars.2017.00108, 2017.

625 Tagliabue, A., Bopp, L., Dutay, J. C., Bowie, A. R., Chever, F., Jean-Baptiste, P., Bucciarelli, E., Lannuzel, D., Remenyi, T.,  
626 Sarthou, G., Aumont, O., Gehlen, M., and Jeandel, C.: Hydrothermal contribution to the oceanic dissolved iron  
627 inventory, *Nat. Geosci.*, 3, 252–256, 2010.

628 Tagliabue, A., Bopp, L., Roche, D. M., Bouttes, N., Dutay, J.-C., Alkama, R., Kageyama, M., Michel, E., and Paillard, D.:  
629 Quantifying the roles of ocean circulation and biogeochemistry in governing ocean carbon-13 and atmospheric  
630 carbon dioxide at the last glacial maximum, *Clim. Past*, 5, 695–706, <https://doi.org/10.5194/cp-5-695-2009>, 2009.

631 Tamburini, F. and Föllmi, K. B.: Phosphorus burial in the ocean over glacial-interglacial time scales, *Biogeosciences*, 6,  
632 501–513, doi:10.5194/bg-6-501-2009, 2009.

633 Tschumi, T., Joos, F., Gehlen, M., and Heinze, C.: Deep ocean ventilation, carbon isotopes, marine sedimentation and the  
634 deglacial CO<sub>2</sub> rise, *Clim. Past*, 7, 771–800, [10.5194/cp-7-771-2011](https://doi.org/10.5194/cp-7-771-2011), 2011.

635 Umling, N. E., and Thunell, R. C.: Mid-depth respired carbon storage and oxygenation of the eastern equatorial Pacific over  
636 the last 25,000 years. *Quaternary Science Reviews*, 189, 43–56, 2018.

637 Vaquer-Sunyer, R. and Duarte, C. M.: Thresholds of hypoxia for marine biodiversity, *Proc. Natl. Acad. Sci.*, 105, 15452–57,  
638 2008.

639 Völker, C. and Tagliabue, A.: Modeling organic iron-binding ligands in a three-dimensional biogeochemical ocean model,  
640 *Mar. Chem.*, 173, 67–77, doi:10.1016/j.marchem.2014.11.008, 2015.

641 Wallmann, K., Schneider, B., and Sarinthein, M.: Effects of eustatic sea-level change, ocean dynamics, and nutrient  
642 utilization on atmospheric *p*CO<sub>2</sub> and seawater composition over the last 130 000 years: a model study, *Clim. Past*,  
643 12, 339–375, <https://doi.org/10.5194/cp-12-339-2016>, 2016.

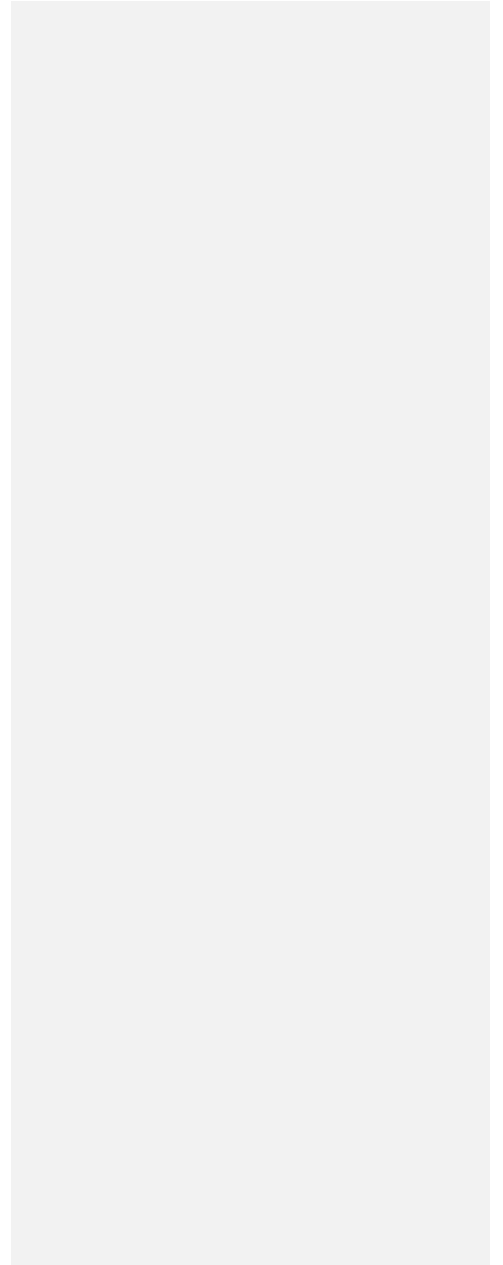
644 Yamamoto, A., Abe-Ouchi, A., Shigemitsu, M., Oka, A., Takahashi, K., Ohgaito, R., and Yamanaka, Y.: Global deep ocean  
645 oxygenation by enhanced ventilation in the Southern Ocean under longterm global warming, *Global Biogeochem.*  
646 *Cy.*, 29, 1801–1815, 2015.

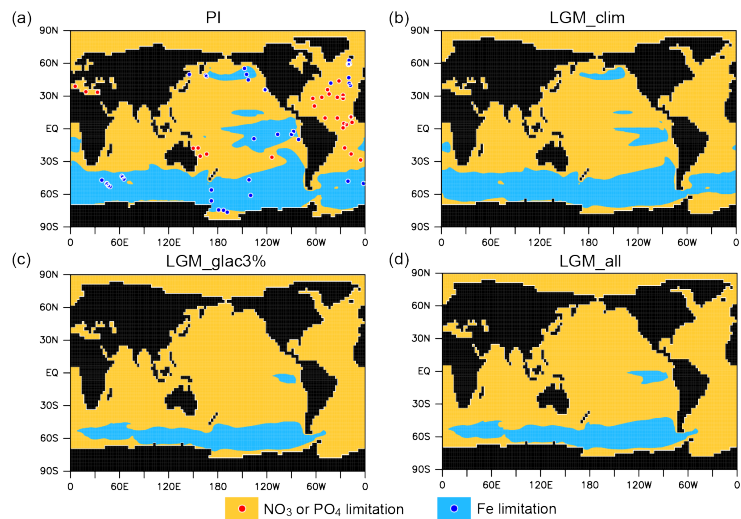
647 Yamamoto, A., Abe-Ouchi, A., and Yamanaka, Y.: Long-term response of oceanic carbon uptake to global warming via  
648 physical and biological pumps, *Biogeosciences*, 15, 4163–4180, <https://doi.org/10.5194/bg-15-4163-2018>, 2018.

649

650

651



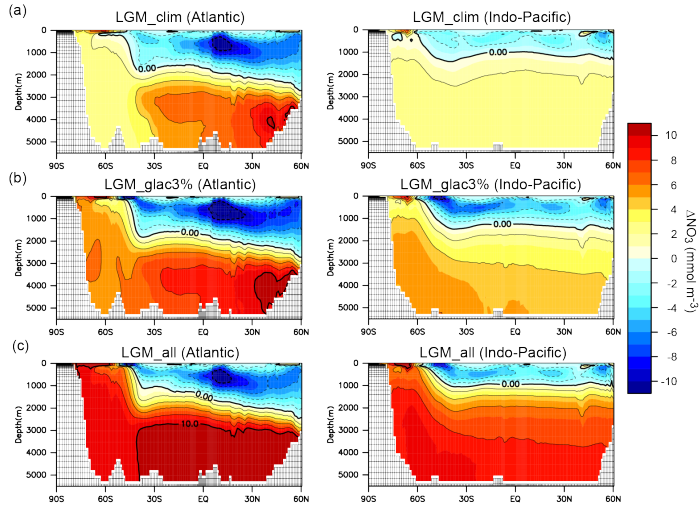


652

653 **Figure 1.** Primary limiting nutrient for phytoplankton for the (a) PI, (b) LGM\_clim, (c) LGM\_glac3%, and (d) LGM\_all.

654 Shade indicates NO<sub>3</sub> or PO<sub>4</sub> limitation (orange) and Fe limitation (blue). Circles represent observed limiting nutrients from  
 655 nutrient addition experiments (Moore et al., 2013).

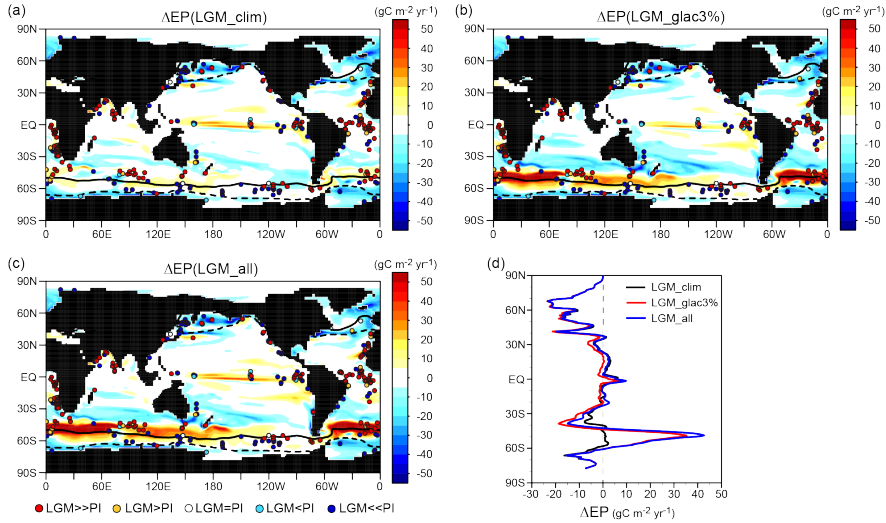
656



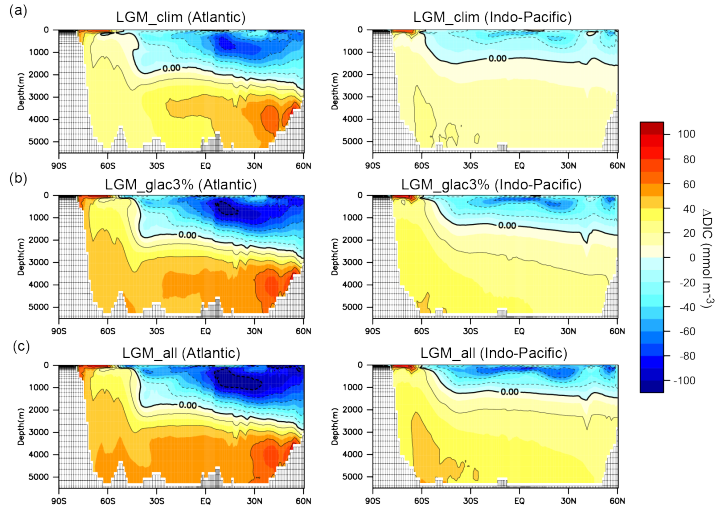
657

658 **Figure 2.** NO<sub>3</sub> change resulting from changes in the climate and biological pump in LGM simulations. Zonal mean changes  
 659 in NO<sub>3</sub> from the PI to (a) LGM\_clim, (b) LGM\_glac3%, and (c) LGM\_all. The left and right panels show the Atlantic and  
 660 Indo-Pacific oceans, respectively.

661

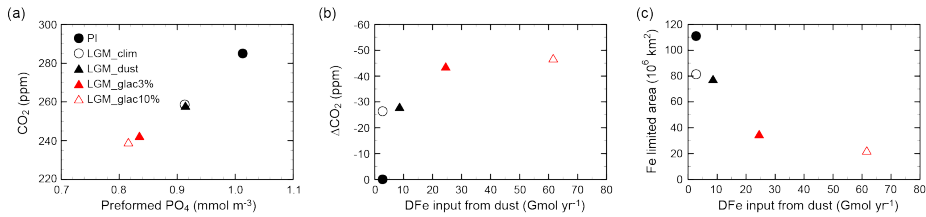


662  
 663 **Figure 3.** Model-proxy comparison of EP change from the PI to LGM. The EP difference from the PI for (a) LGM\_clim, (b)  
 664 LGM\_glac3%, and (c) LGM\_all. Circles show proxy data (Kohfeld et al., 2013). Solid (dotted) lines refer to the glacial sea  
 665 ice fraction of 0.1 during August (February). (d) Zonal mean changes in the surface EP from the PI for LGM\_clim (black),  
 666 LGM\_glac3% (red), and LGM\_all (blue).  
 667



668  
 669 **Figure 4.** DIC change resulting from changes in the climate and biological pump in LGM simulations. Zonal mean changes  
 670 in DIC from PI to (a) LGM\_clim, (b) LGM\_glac3%, and (c) LGM\_all. The left and right panels show the Atlantic and Indo-  
 671 Pacific oceans, respectively.

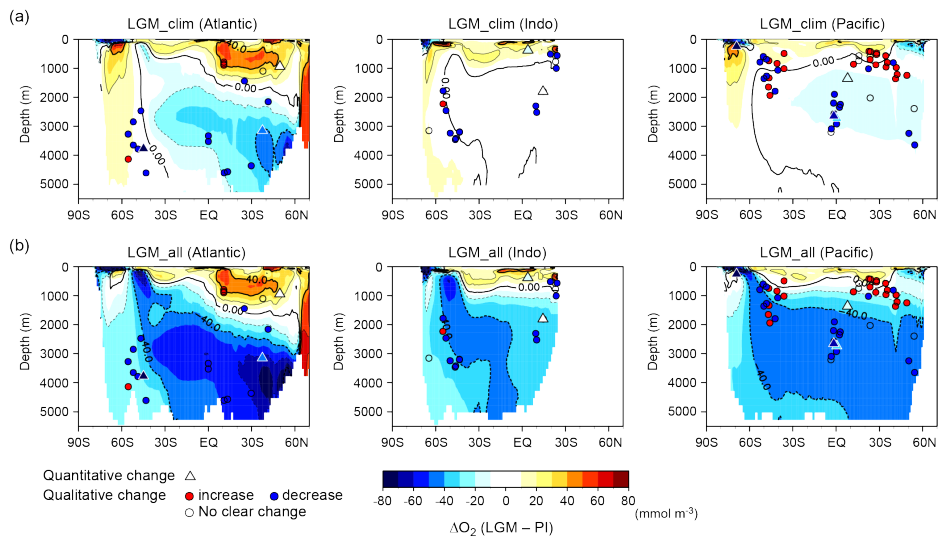
672



673  
 674 **Figure 5.** CO<sub>2</sub> change and its relationship to efficiency of the biological pump and iron cycle. (a) Atmospheric CO<sub>2</sub> as a  
 675 function of globally averaged preformed PO<sub>4</sub>. (b) Changes in CO<sub>2</sub> from the PI as a function of DFe input from dust. (c) Fe-  
 676 limited area as a function of DFe input from dust. Shown are the PI (black filled circle), LGM\_clim (black open circle),  
 677 LGM\_dust (black filled triangle), LGM\_glac3% (red filled triangle), and LGM\_glac10% (red open triangle).

678

679

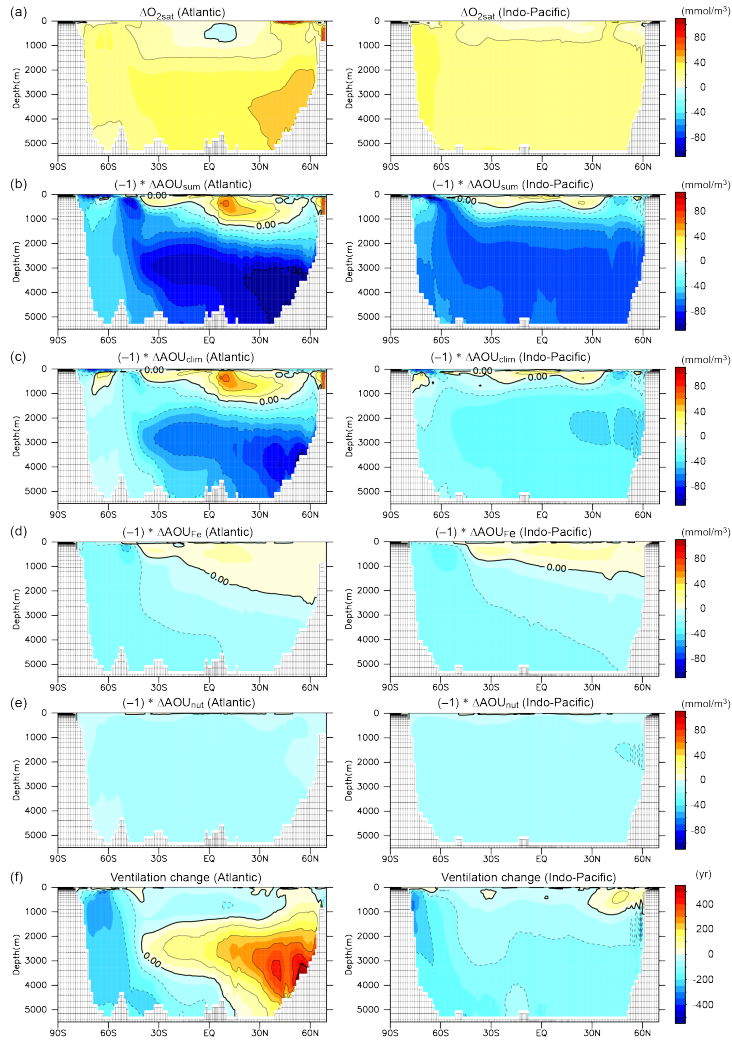


680

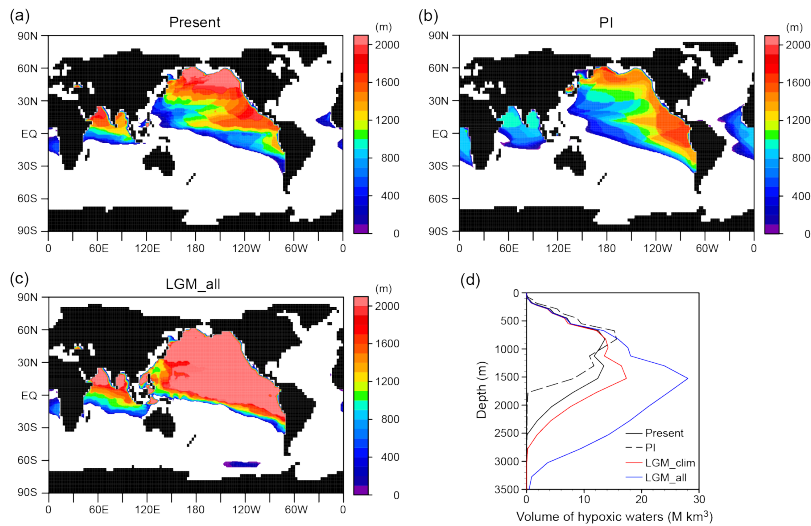
681 **Figure 6.** Model-proxy comparison of changes in dissolved oxygen concentration from the PI to LGM. Zonal mean changes  
682 in  $O_2$  from the PI to (a) LGM\_clim and (b) LGM\_all for the Atlantic (left), Indian (middle), and Pacific (right) oceans; the  
683 contour interval is  $20 \text{ mmol m}^{-3}$ . Circles show proxy records of qualitative  $O_2$  change from multi-proxy data compilation from  
684 Jaccard and Galbraith (2012) (except  $\delta^{15}\text{N}$  data), Jaccard et al. (2016), and Durand et al. (2018). Red (blue) circles indicate  $O_2$   
685 increase (decrease) from the Holocene to LGM. Triangles show proxy records of quantitative  $O_2$  change from (Schmiedl and  
686 Mackensen, 2006; Hoogakker et al., 2015, 2018; Gottschalk et al., 2016; Lu et al., 2016; Bunzel et al., 2017; Umling and  
687 Thunell, 2018) (triangles shaded using the same colour scale).

688

689



691 **Figure 7.** Contributions of individual mechanisms to oxygen change and ventilation change. Zonal mean changes of (a)  $O_{2sat}$ ,  
 692 (b)  $AOU_{sum}$ , (c)  $AOU_{clim}$ , (d)  $AOU_{Fe}$ , (e)  $AOU_{nut}$ , and (f) ventilation age from the PI to LGM. Left and right panels show the  
 693 Atlantic and Indo-Pacific oceans: the contour intervals are  $20 \text{ mmol m}^{-3}$  for (a)–(e) and 100 years for (f). We decomposed the  
 694 total AOU change ( $\Delta AOU_{sum} = AOU_{(LGM\_all)} - AOU_{(PI)}$ ) into the effects of climate change ( $\Delta AOU_{clim} = AOU_{(LGM\_clim)} -$   
 695  $AOU_{(PI)}$ ), iron fertilization ( $\Delta AOU_{Fe} = AOU_{(LGM\_glac3\%)} - AOU_{(LGM\_clim)}$ ), and nutrient inventory increase ( $\Delta AOU_{nut} =$   
 696  $AOU_{(LGM\_all)} - AOU_{(LGM\_glac3\%)}$ ).  
 697



698 **Figure 8.** Hypoxic waters expansion. Horizontal distribution of thickness of the hypoxic waters ( $[O_2] < 80 \text{ mmol m}^{-3}$ ) for the  
 699 (a) present, (b) PI, and (c) LGM\_all. (d) Vertical distribution of hypoxic waters for the present (black solid), PI (black dashed),  
 700 LGM\_clim (red), and LGM\_all (blue). Because current coarse resolution models have difficulties reproducing low oxygen  
 701 concentration for the present day (Bopp et al., 2013), observed values from WOA2009 (Garcia et al., 2010a) were used for the  
 702 present. For the LGM simulations, we combined the observed values with the modelled changes.  
 703  
 704

| Experiments | Climate | Dust deposition | Fe solubility in glaciogenic dust | Dust DFe (Gmol yr <sup>-1</sup> ) | Global PO <sub>4</sub> (mmol m <sup>-3</sup> ) |
|-------------|---------|-----------------|-----------------------------------|-----------------------------------|--|
| PI          | PI      | PI              | -                                 | 2.7                               | 2.13   |
| LGM_clim    | LGM     | PI              | -                                 | 2.7                               | 2.2 (+3%)                                      |
| LGM_dust    | LGM     | LGMctl          | -                                 | 8.6                               | 2.2 (+3%)                                      |
| LGM_glac3%  | LGM     | LGMglac         | 3%                                | 24.5                              | 2.2 (+3%)                                      |
| LGM_glac10% | LGM     | LGMglac         | 10%                               | 61.6                              | 2.2 (+3%)                                      |
| LGM_all     | LGM     | LGMglac         | 3%                                | 24.5                              | 2.45 (+15%)                                    |

705

706 Table 1. Description of the model experiments.

707

| Experiments | Surface NO <sub>3</sub> (mmol m <sup>-3</sup> ) | Surface DFe (μmol m <sup>-3</sup> ) | Fe limited area (10 <sup>6</sup> km <sup>2</sup> ) | Global ΔEP (Pg C yr <sup>-1</sup> ) | ΔEP (>45°S) (Pg C yr <sup>-1</sup> ) | ΔEP (<45°S) (Pg C yr <sup>-1</sup> ) | Preformed PO <sub>4</sub> (mmol m <sup>-3</sup> ) | ΔCO <sub>2</sub> (ppm) | ΔO <sub>2</sub> <sub>deep</sub> (mmol m <sup>-3</sup> ) | ΔAOU <sub>deep</sub> (mmol m <sup>-3</sup> ) |
|-------------|---|-------------------------------------|--|-------------------------------------|--------------------------------------|--------------------------------------|---|------------------------|---|--|
| PI          | 7.7   | 0.38                                | 111  | (8.54)                              | (6.19)                               | (2.35)                               | 1.013   | (285)                  | (156)   | (182.5)                                      |
| LGM_clim    | 6.8   | 0.39                                | 81   | -0.54                               | -0.45                                | -0.09                                | 0.913   | -26.4                  | -7  | 37.3   |
| LGM_dust    | 6.9   | 0.42                                | 80   | -0.54                               | -0.49                                | -0.05                                | 0.914   | -27.6                  | -8  | 38.9   |
| LGM_glac3%  | 5.8   | 0.5                                 | 35   | -0.54                               | -1.31                                | +0.77                                | 0.835   | -43.2                  | -28   | 58.7   |
| LGM_glac10% | 5.5   | 0.54                                | 23   | -0.54                               | -1.46                                | +0.92                                | 0.816   | -46.4                  | -33   | 63.6   |
| LGM_all     | 6.5   | 0.48                                | 39   | +0.32                               | -0.63                                | +0.95                                | 1.002   | -59.2                  | -42   | 72.8   |

708

709 Table 2. Results of the model experiments. Simulated global average of surface NO<sub>3</sub>, DFe, and Fe-limited area and changes in

710 EP at 100 m, atmospheric CO<sub>2</sub>, and globally averaged preformed PO<sub>4</sub>, O<sub>2</sub> and AOU below 2000 m depth from the PI. Values

711 in brackets are the PI results.